Published in CEAS Space Journal 9, issue 4, 493-505, 2017
which should be used for any reference to this work

All-fiber versatile laser frequency reference at 2 μm for CO_2 space-borne lidar applications

Stéphane Schilt[1] · Renaud Matthey[1] · Kenny Hey Tow[2] · Luc Thévenaz[2] · Thomas Südmeyer[1]

Abstract We present a frequency stabilized laser at 2051 nm based on a versatile all-fibered stabilization setup. A modulation sideband locking technique is implemented to lock the laser at a controlled frequency detuning from the center of the CO_2 R(30) transition envisaged for space-borne differential absorption lidar (DIAL) applications. This method relies on the use of a compact all-fibered gas reference cell that makes the setup robust and immune to mechanically induced optical misalignments. The gas cell is fabricated using a hollow-core photonic crystal fiber filled with pure CO_2 at a low pressure of ~20 mbar and hermetically sealed at both ends by splices to silica fibers. Different configurations of this fibered cell have been developed and are presented. With this technique, frequency stabilities below 40 kHz at 1-s integration time and <100 kHz up to 1000-s averaging time were achieved for a laser detuning by around 1 GHz from the center of the CO_2 transition. These stabilities are compliant with typical requirements for the reference seed source for a space CO_2 DIAL.

Keywords Laser stabilization · Lidar · Sideband locking · Hollow-core photonic crystal fiber · Optical standards and testing · Molecular spectroscopy

This paper is based on a presentation at the International Conference on Space Optics (ICSO), 18–21 October, 2016, Biarritz, France.

✉ Stéphane Schilt
stephane.schilt@unine.ch

[1] Laboratoire Temps-Fréquence, Université de Neuchâtel, Avenue de Bellevaux 51, 2000 Neuchâtel, Switzerland

[2] EPFL Swiss Federal Institute of Technology, Institute of Electrical Engineering, SCI-STI-LT, Station 11, 1015 Lausanne, Switzerland

1 Introduction

Sensing atmospheric gas traces is crucial for climate monitoring and to predict the importance of global climate changes. Among the various atmospheric constituents, carbon dioxide (CO_2), methane (CH_4) and water vapor (H_2O-v), the most prominent greenhouse gasses, have a major impact on climate. Advanced monitoring techniques are necessary to measure these gas species on a global scale all around the Earth. In the case of CO_2, improved accuracy and precision would enable determining more correctly its source and sink locations, its amount and variability, to better understand its fluxes and exchanges between the atmosphere, the lands and the oceans, and, hence, its global cycle. The global coverage and spatial resolution that are generally required for such a monitoring have driven the studies of space-borne active remote sensing Light Detection and Ranging (lidar) instruments [1]. A lidar relies on a time-resolved analysis using short laser light pulses scattered back to the instrument by atmospheric constituents or by a solid surface (e.g., the ground surface for airborne lidars) to measure the density profile of the studied species or its integrated column density [2]. The Differential Absorption Lidar (DIAL) approach offers the advantage of selective detection of the target species by sensing the difference in light absorption at two close wavelengths, one of which is chosen to coincide with an absorption line of the species under study, whereas the second one is chosen sufficiently far off the line to avoid substantial absorption [3].

Being the most important anthropogenic greenhouse gas and the prominent contributor to the total anthropogenic change in the Earth radiation budget, CO_2 is of particular interest in the context of global climate warming. This is why space agencies have been studying future CO_2 space-borne integrated-path differential absorption (IPDA) lidar

instruments [4], e.g., for the envisaged missions Advanced Space Carbon and climate Observation of Planet Earth (A-SCOPE) by ESA [5] and Active Sensing of CO_2 Emissions over Nights, Days and Seasons (ASCENDS) by NASA [4]. Space-borne IPDA lidars have the potential to perform measurements of the total vertical CO_2 column with the necessary precision and accuracy to fulfill the goals of these scientific missions. Two appropriate wavelength ranges were identified at 1.57 and 2.05 μm. The 1.57-μm spectral range is technologically more mature as it benefits from active and passive photonics components developed for the optical fiber telecommunications. However, the 2.05-μm region is more favorable from a spectroscopic point-of-view, since the absorption cross-section is substantially larger, allowing the on-line wavelength to be tuned to a value offering higher sensitivity to the CO_2 concentration in the lower troposphere, near to the Earth's surface, where all CO_2 sources are located [6]. The R(20) transition in the $(2\nu_1 + 2\nu_2 + \nu_3)$ vibrational band at 1572 nm and the R(30) transition in the $(4\nu_2 + \nu_3)$ band at 2051 nm were identified as promising candidate absorption lines for an IPDA lidar mission. They exhibit in particular a small temperature sensitivity and low interference with water vapor [6, 7], which are necessary conditions to minimize the impact of these parameters onto the measurement of the CO_2 optical depth. The water vapor dependency may be further limited or even suppressed by an adequate selection of the off-line frequency, in such a way that it shows the same water vapor absorption level as the on-line frequency [8].

The performance of IPDA lidar systems is notably determined by the spectral purity, accuracy and frequency stability of a low-power continuous-wave (cw) laser that seeds the high-power pulsed laser transmitter. These properties are especially important for the on-line wavelength, which is generally detuned from the center of the probed molecular absorption line by a given frequency offset. A precise control of the frequency detuning of the seed laser is thus needed in a spectral range covering a few gigahertz around the center of the transition. Simultaneously, high frequency stability and accuracy of the laser are required. It has been mentioned that an Allan deviation [9] of 20–110 kHz for integration times longer than 700 s is required at a wavelength of 1572 nm, whereas this condition is relaxed to 70–400 kHz at 2.05 μm (to enable CO_2 concentration determination with a systematic error level below 0.05–0.15 ppm) [10]. These values represent upper limits to the magnitude of mid-term frequency fluctuations. Larger values resulting from white noise over shorter integration times are tolerable.

In the wavelength range around 1560 nm, high frequency stability can be achieved by combining a frequency-doubling process with frequency stabilization to a rubidium (Rb) transition at 780 nm. To transfer the high frequency stability of Rb-locking into a large spectral range centered at 1.56 μm, the use of an electro-optic modulator (EOM) frequency comb pumped by a Rb-stabilized master laser has been demonstrated [11]. The EOM comb was used to bridge the spectral gap between a 1572-nm slave laser and the 1560-nm master laser. Thus, a frequency stability of 2 kHz has been achieved at 1572 nm for an integration time of 1 s. This value is improved to less than 800 Hz for integration times ranging from 1 h up to 3 days [12]. Unfortunately, this approach cannot be immediately implemented at 2 μm due to the lack of technology (no EOM comb is available at this wavelength) and to the absence of a suitable atomic transition reachable through a non-linear process, thereby requiring a direct stabilization to a CO_2 transition. The drawback is that CO_2 transitions are much weaker and spectrally broader than the sub-Doppler atomic Rb absorption line used in the aforementioned 1572-nm laser stabilization scheme (where the considered transition linewidth was in the range of 15 MHz). Therefore, root-mean-square (rms) frequency deviations of several hundred kilohertz have typically been reported so far for cw lasers frequency-stabilized to Doppler-broadened CO_2 transitions at 2053 nm [R(22) line] [13] or 2051 nm [R(30) line] [14].

Stabilizing a laser at a frequency detuned from the center of a molecular transition can be achieved using a side-of-fringe locking scheme [15]. However, this method suffers from its sensitivity to amplitude variations that are transposed to frequency fluctuations, and from the impossibility to precisely control the absolute offset frequency. Another common approach for a frequency-detuned locking is a master–slave configuration, in which a master laser is stabilized to the center of the considered transition and a slave laser is offset-locked with respect to the master laser. The offset-lock can be achieved by a phase-lock loop or by a frequency offset-lock [16]. These methods have proven their efficiency to transfer the frequency stability of the master to the slave laser. Using such a scheme, frequency stabilization of a (slave) cw laser to the side of a CO_2 transition at 2053 nm was for instance realized for further injection seeding of a pulsed oscillator [13]. However, two distinct laser sources are needed, each with its own driving electronics, which can be a drawback in some conditions, e.g., for space applications.

In this article, we present a different approach for laser frequency stabilization with an offset frequency from the center of the R(30) transition of CO_2 at 2051 nm based on a versatile modulation sideband locking scheme. The proposed method enables the laser to be directly locked at an adjustable frequency detuning, without using a master–slave configuration. The principle basically consists of modulating the phase or amplitude of the laser radiation using a broadband modulator (e.g., an EOM) to generate

sidebands, one of which being stabilized to the center of the molecular transition. The carrier frequency is then precisely set by changing the frequency used to generate the sideband, thus locking the unmodulated laser at the target frequency detuning. A similar method has been previously implemented to stabilize a modulation sideband to a narrow sub-Doppler molecular transition obtained by saturation spectroscopy [17] or to the narrow resonance of a Fabry–Perot cavity [18, 19]. Here, we have investigated the possibility to apply this approach for the first time in the 2-μm spectral range and with a wider Doppler-broadened absorption feature, which brings additional challenges. Since parameters like weight and size are of prime importance for space applications, this motivated the fabrication of a compact gas reference cell made of a hollow-core photonic crystal fiber (HC-PCF) [20]. The HC-PCF was filled with pure CO_2 at low pressure (~20 mbar) and sealed at both ends by splices to silica fibers, which resulted in a robust all-fiber setup that is immune to mechanically induced optical misalignments [21, 22].

This article starts with a general presentation of the principle of our proposed frequency locking scheme (Sect. 2). The fabrication technique of the all-fiber CO_2 reference cells made of an HC-PCF is thoroughly described in Sect. 3. Finally, we report in Sect. 4 experimental results related to various aspects of the developed laser frequency reference and locking system (FRLS).

2 Modulation sideband locking

2.1 Experimental setup and basic principle

Figure 1 shows the principle of our proposed modulation sideband locking. The setup is entirely fiber-coupled; polarization-maintaining (PM) fibers, optimized for operation at 2 μm (e.g., Nufern PM-1950 fiber), are used to ensure a stable polarization and to minimize optical losses due to fiber bending since the optical setup is enclosed in a compact breadboard demonstrator of dimensions 25 cm × 25 cm × 5 cm. A distributed feedback (DFB) laser (from Nanoplus GmbH) delivering an output power of more than 15 mW at a wavelength of 2.05 μm is used as a single-frequency light source. The setup requires an external fiber isolator providing an additional >35-dB isolation rate despite the presence of a single-stage optical isolator in the laser butterfly package (with a typical isolation of 40 dB). The reason is that the laser was subjected to strong frequency fluctuations and jumps, in the order of 50 MHz over a few seconds, resulting from optical feedback without this additional isolator. After the isolator, the output light is divided into two paths by a 1 × 2 fiber splitter with a splitting ratio of 85/15. The higher power branch is used

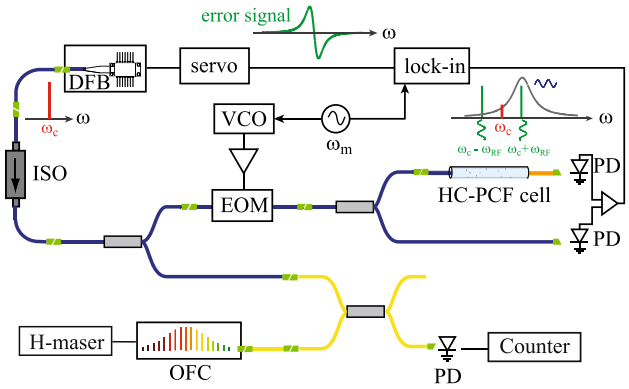

Fig. 1 Schematic representation of the modulation sideband locking for off-center stabilization of a DFB laser emitting at frequency ω_c to a molecular transition. Modulation sidebands with a frequency separation ω_{RF} from the laser carrier, which corresponds to the targeted detuning from the absorption line center, are created using an EOM driven by a VCO. The sidebands are represented by the *green lines* in the schematic EOM optical spectrum, whereas the *red line* shows the laser carrier. *ISO* isolator, *PD* photodetector, ω_m modulation frequency. *Colored lines* represent optical fibers (*blue* PM, *yellow* SM, *orange* MM). The frequency stability of the locked laser is evaluated from the heterodyne beat with a fully stabilized optical frequency comb (OFC) as schematized in the *bottom part* of the figure

as a frequency-stable output of the system, while the other one with less than 2 mW is used for frequency stabilization. A broadband intensity EOM (Photline MPZ-LN-01) is used to generate twinned sidebands, one of which is stabilized to the center of the considered R(30) transition in the $(4\nu_2 + \nu_3)$ vibrational band of CO_2 at 2051 nm using a feedback loop. Hence, the frequency of the laser carrier can be precisely set by changing the radio-frequency (RF) used to generate the sidebands, thereby locking it at the target frequency detuning. The frequency stabilization of the sideband is performed by wavelength modulation spectroscopy (WMS) [23]. This is done by applying a sinusoidal frequency modulation to the EOM driving signal, supplied by a voltage-controlled oscillator (VCO), as mathematically described in the next section. An error signal is obtained by demodulating the optical signal transmitted through a CO_2 reference gas cell at the VCO modulation frequency (first harmonic demodulation). A feedback signal for laser stabilization is finally applied to the laser injection current. The laser control electronics (low-noise current source and temperature controller), the modulation–demodulation for the generation of the error signal and the proportional–integral (PI) servo controller to close the feedback loops are all enclosed in a home-made laser controller. To reduce the amplitude modulation resulting from the modulation of the VCO control voltage, which distorts the error signal, a balanced detection is implemented using a 1 × 2 fiber splitter and a pair of 300-μm diameter extended-InGaAsP photodiodes with a cut-off wavelength of 2.1 μm. To minimize

the variations of the reference cell background transmission induced by temperature variations, the cell is enclosed in a temperature-regulated housing (see Sect. 3.4).

2.2 Mathematical description

The developed modulation sideband locking scheme requires the generation of a spectral sideband from the laser carrier, at an offset frequency in the range of some hundred megahertz to a few gigahertz. This can be efficiently performed using an EOM. In the optical telecommunications wavelength range of 1.55 μm, single-sideband (SSB) EOMs are commercially available, which enable a unique sideband to be generated. This is an optimal configuration since a maximum optical power can be transferred into a single sideband, which can be locked to the considered molecular transition without any perturbation induced by the presence of spurious sidebands. The use of an SSB-EOM in a similar configuration has been demonstrated in the near-infrared spectral region of 1.59 μm for the realization of a continuously tunable laser source with a narrow linewidth and precise frequency control by sideband locking to a high-finesse optical cavity [24]. However, such a component is not available in the wavelength range of 2 μm. Therefore, a standard EOM must be used, which produces additional sidebands that can impact the stabilization by inducing spurious contributions to the error signal. An intensity EOM has been preferentially used as it allows the incident optical power to be split among only one pair of sidebands. In contrast, a phase EOM either presents more than one pair of sidebands or has a large fraction of the optical power remaining in the carrier, depending on the modulation index.

An intensity EOM consists of a Mach–Zehnder interferometer, in which a phase shift $\pm\phi(t)$ is applied in each branch. This phase shift comprises a DC component ϕ_0 that can be controlled by the bias voltage V_{bias} applied to the EOM and an AC component $\phi_{\text{RF}}(t) = \beta \sin \omega_{\text{RF}} t$ induced by the RF signal $V_{\text{RF}}(t) = V_{\text{RF},0} \sin \omega_{\text{RF}} t$ applied to the EOM electrodes, where β is the modulation index and ω_{RF} the driving RF. The RF phase shift can be written as a function of the V_π value of the EOM, i.e., the amplitude of the RF signal that induces a phase shift of π between the two arms of the interferometer:

$$\beta = \pi V_{\text{RF},0} \big/ (2V_\pi). \tag{1}$$

The phase shift produced in the two arms is of opposite sign, which results in a doubled relative shift $2\phi(t) = 2\phi_0 + 2\beta \sin \omega_{\text{RF}} t$ between the two corresponding waves $E_1(t)$ and $E_2(t)$ that are recombined at the output of the interferometer to produce the output electrical field $E_{\text{EOM}}(t)$. To implement WMS with one of the sidebands for its frequency stabilization to a molecular transition, we frequency-modulated the RF signal driving the EOM at an angular frequency ω_{m} and with a modulation depth $\Delta\omega_{\text{RF}}$:

$$V_{\text{RF}}(t) = V_{\text{RF},0} \sin\left[\omega_{\text{RF}} + \Delta\omega_{\text{RF}} \sin(\omega_{\text{m}} t)\right] t. \tag{2}$$

We implemented this frequency modulation by driving the EOM with the RF signal delivered by a VCO with a center frequency corresponding to ω_{RF}, and by modulating its control voltage at frequency ω_{m}: $V_{\text{contr}}(t) = V_0 + \Delta V \sin(\omega_{\text{m}} t)$. The resulting electrical field at the output of the EOM is given by:

$$E_{\text{EOM}}(t) = \frac{E_1(t) + E_2(t)}{\sqrt{2}} = \frac{E_0}{2} \mathrm{e}^{i\omega_c t} \Big[\mathrm{e}^{i\phi_0} \mathrm{e}^{i\beta \sin\left[\omega_{\text{RF}} + \Delta\omega_{\text{RF}} \sin(\omega_{\text{m}} t)\right] t} + \mathrm{e}^{-i\phi_0} \mathrm{e}^{-i\beta \sin\left[\omega_{\text{RF}} + \Delta\omega_{\text{RF}} \sin(\omega_{\text{m}} t)\right] t} \Big]. \tag{3}$$

Here, E_0 and ω_{c} are the amplitude and angular frequency, respectively, of the laser carrier. Using the Fourier series expansion $\mathrm{e}^{\mp i\beta \sin \omega t} = \sum_n (-1)^n J_n(\beta)\, \mathrm{e}^{\pm in\omega t}$, where $J_n(\beta)$ is the ordinary Bessel function of order n, the electrical field at the EOM output can be written as:

$$E_{\text{EOM}}(t) = \frac{E_0}{2} e^{i\omega_c t} \Bigg[\mathrm{e}^{i\phi_0} \sum_n (-1)^n J_n(\beta)\, \mathrm{e}^{-in\omega_{\text{RF}} t} \mathrm{e}^{-in\left[\Delta\omega_{\text{RF}} \sin(\omega_{\text{m}} t)\right] t} + \mathrm{e}^{-i\phi_0} \sum_n (-1)^n J_n(\beta)\, \mathrm{e}^{in\omega_{\text{RF}} t} \mathrm{e}^{in\left[\Delta\omega_{\text{RF}} \sin(\omega_{\text{m}} t)\right] t} \Bigg]. \tag{4}$$

We consider here the case $\beta \ll 1$ that usually occurs in an EOM, such that only the first pair of sidebands ($n = \pm 1$) has a relevant magnitude:

$$E_{\text{EOM}}(t) = E_0 \Big[J_0(\beta) \cos\phi_0 \mathrm{e}^{i\omega_c t} - iJ_1(\beta) \sin\phi_0 \mathrm{e}^{i\left[\omega_c - \omega_{\text{RF}} - \Delta\omega_{\text{RF}} \sin(\omega_{\text{m}} t)\right] t} + iJ_1(\beta) \sin\phi_0 \mathrm{e}^{i\left[\omega_c + \omega_{\text{RF}} + \Delta\omega_{\text{RF}} \sin(\omega_{\text{m}} t)\right] t} \Big]. \tag{5}$$

Therefore, the optical signal at the output of the EOM is made of the unmodulated carrier at ω_{c} with two sidebands centered at $\omega_{\text{c}} \pm \omega_{\text{RF}}$ that are frequency-modulated with a modulation depth $\Delta\omega_{\text{RF}}$. These sidebands act like two distinct frequency-modulated single mode lasers. The WMS technique [23] can thus be implemented with each of these sidebands to generate a derivative-like signal of a molecular absorption line for frequency stabilization by first-harmonic demodulation. To maximize the optical power in the two sidebands, the DC bias voltage of the EOM is tuned to suppress the carrier (corresponding to $\phi_0 = \pi/2$ in Eq. 5) and the RF power is adjusted accordingly. In this case, the optical intensity at the output of the EOM is:

$$I_{\mathrm{EOM}}(t) = |E_{\mathrm{EOM}}(t)|^2 = 2E_0^2 J_1^2(\beta)[1 - \cos(2(\omega_{\mathrm{RF}} + \Delta\omega_{\mathrm{RF}} \sin\omega_{\mathrm{m}} t)\, t)]. \quad (6)$$

The maximum relative power that can be transferred in each sidebands is around 35% (corresponding to the maximum value of $|J_1(\beta)|^2$). Even if the carrier is not properly suppressed, there is no impact on the WMS signal, as the carrier is not modulated. Therefore, it does not contribute to the derivative demodulated signal.

Besides the frequency modulation (FM) required to generate the WMS signal for sideband locking, the modulation of the VCO control voltage also induces an amplitude modulation (AM) of the optical signal at the output of the EOM. A first reason to this AM signal directly results from the phase-shifted FM occurring in the two arms of the EOM, which produces a characteristic fringes pattern (linked to the term $\Delta\omega_{\mathrm{RF}}(\sin\omega_{\mathrm{m}}t)$ in the cosine expression in Eq. 6) when the two waves are recombined at the EOM output.

A second contribution to the AM signal arises from the imperfect behavior of the VCO, whose output power slightly varies during the modulation cycle. Therefore, the amplitude $V_{\mathrm{RF},0}$ of the RF signal (2) that drives the EOM is not constant, which induces a variation of the modulation index β according to (1) and, consequently, of the EOM output intensity according to (6). This so-called residual amplitude modulation (RAM) [25] produces an offset in the demodulated WMS signal, inducing a shift of the zero-crossing point of the first-harmonic error signal from the center of the absorption line. To circumvent this effect, a balanced detection is implemented using the signal of a reference detector at the output of the EOM (see Fig. 1).

3 HC-PCF reference gas cells

Regarding space applications, parameters such as the weight, size, ruggedness, or insensitivity to vibrations, are of prime importance. Holey fibers, more particularly hollow-core fibers, constitute an excellent geometry to create light-gas interactions in a very confined medium. In these micro-structured fibers, light is not guided by total internal reflection as in standard optical fibers, but in general by a photonic bandgap in the cladding that acts like a barrier for light [20]. As the guiding mechanism is no longer dependent on the core refractive index, it is possible to design fibers that guide light in a hollow core. Filling this hollow core with a specific gas enables a very high gas–light interaction (overlap ratio >95%) as most of the optical power propagates in the core. This gives rise to the realization of very compact reference gas cells with long optical pathlengths in a small form factor. However, HC-PCFs also present some drawbacks such as (1) intermodal interference noise resulting from the simultaneous propagation of several optical modes for HC-PCFs with a core diameter compatible with standard single mode (SM) fibers, (2) the difficulty to be fusion-spliced to standard silica fibers owing to the high sensitivity of the thin silica web to heating, or (3) the presence of interferometric noise caused by back-reflections at both ends of the HC-PCF that result from the large refractive index contrast between silica and air when an HC-PCF is spliced to solid-core fibers to make a sealed gas cell.

3.1 Optimization of the cell parameters

We defined the parameters (filling pressure, pathlength) of the reference CO_2 fiber cell to be used for laser stabilization with the aim of maximizing the slope of the error signal. Numerical calculations were performed to determine the shape of the CO_2 R(30) absorption line and the corresponding error signal based on the spectroscopic parameters of the HITRAN 2008 database [26] that are listed in Table 1. The dependence of the line center absorption and linewidth of the absorption profile as a function of the cell length is shown in Fig. 2 for different CO_2 pressures. From these results, a fiber length of 3 m with a CO_2 pressure of ~20 mbar have been selected as they lead to a minor broadening of the CO_2 line compared to the Doppler width of 270 MHz, and to a reasonable length for the cell fabrication.

For the selected HC-PCF length of 3 m, Fig. 3 displays the slope of the error signal as a function of the sideband modulation depth ($\Delta\omega_{\mathrm{RF}}$ in Eq. 2) and of the CO_2 pressure. For this length, the maximum slope of the error signal is obtained for a modulation depth of ~220 MHz and a CO_2 pressure of ~16 mbar. With a slightly higher CO_2 pressure of 20 mbar, the decrease in the slope of the error signal

Table 1 Spectroscopic parameters of the CO_2 R(30) transition used for frequency stabilization according to HITRAN2008 database [26]

Transition	ν_{vac} (cm^{-1})	λ_{vac} (nm)	S ($\mathrm{cm}^{-1}/(\mathrm{mol\ cm}^{-2})$)	g_{air} ($\mathrm{cm}^{-1}\ \mathrm{atm}^{-1}$)	g_{s} ($\mathrm{cm}^{-1}\ \mathrm{atm}^{-1}$)	E'' (cm^{-1})	n	δ_{air} ($\mathrm{cm}^{-1}\ \mathrm{atm}^{-1}$)
R(30)	4875.74873	2050.967	1.74×10^{-22}	0.0684	0.0869	362.7883	0.78	7.0×10^{-3} [27]

ν_{vac} vacuum wavenumber, λ_{vac} vacuum wavelength, S line strength, g_{air} air-broadened half-width, g_s self-broadened half-width, E'' lower state energy, n temperature-dependence exponent for g_{air}, δ_{air} air pressure-induced line shift

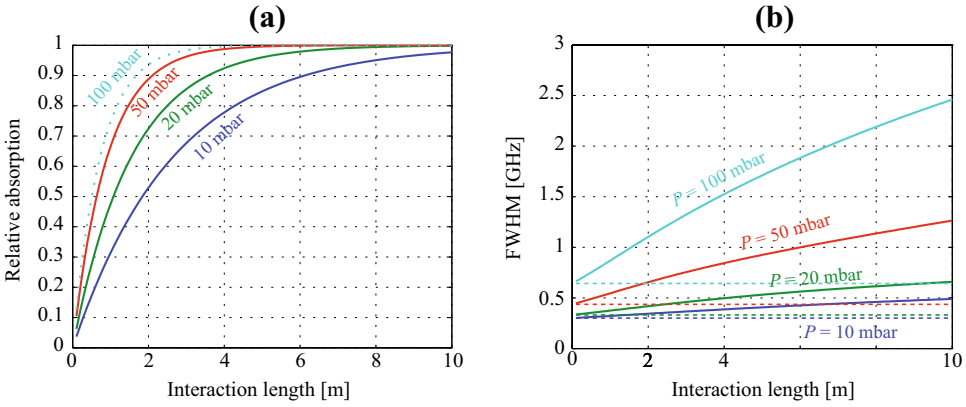

Fig. 2 **a** Relative absorption at the center of the CO_2 R(30) transition obtained as a function of the optical pathlength at different gas pressures (pure CO_2). **b** Full width at half maximum (FWHM) of the corresponding absorption profile as a function of the absorption length at different gas pressures. For comparison, the *dashed lines* represent the Voigt linewidth of the transition. The additional broadening compared to this value arises from the non-linear behavior of the Beer–Lambert law in the considered regime of high absorption

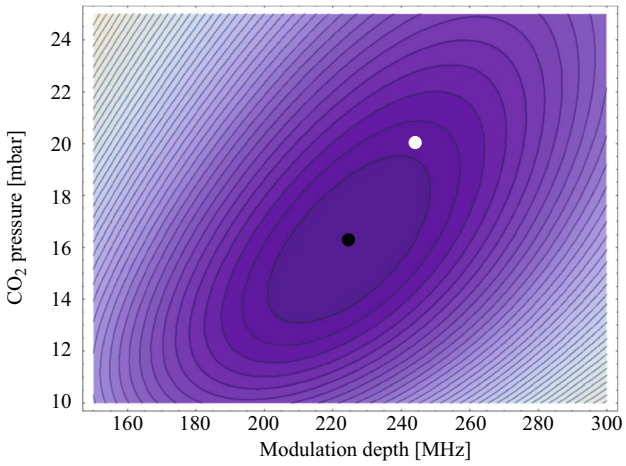

Fig. 3 Example of a contour plot displaying the slope of the error signal as a function of the modulation depth (*horizontal axis*) and the gas pressure (*vertical axis*) obtained for a 3-m HC-PCF. Each contour corresponds to a change of about 1% of the maximum value obtained at a pressure of ~16 mbar and a modulation depth of ~220 MHz (*black point*). The *white point* shows the planned experimental conditions with a nominal cell pressure of 20 mbar

is minor, less than 2% at the optimal modulation depth of ~240 MHz. Even in a larger span of modulation depths ranging from 200 to 300 MHz, the calculated slope of the error signal is reduced by less than 10% from its maximum value.

3.2 HC-PCF cell fabrication

The fabrication process of our all-fiber CO_2 cell is schematized in Fig. 4. It relies on the permeation of gaseous helium through the walls of the silica fiber [28] to fabricate low-pressure gas cells that can be sealed by a fusion splice performed at ambient pressure conditions without contamination of the cell by the surrounding air. For the realization of CO_2 reference cells at 2 μm, we used the hollow core fiber HC-2000-01 (from NKT Photonics). Its mode field diameter is around 11 μm and its cross-section is depicted in the center of Fig. 4.

The fabrication process starts by connectorizing one end of the HC-PCF by a fusion splice to a SM fiber patchcord. The "pigtailed" HC-PCF is then placed in a hermetic vacuum chamber equipped with optical fibers and electrical feedthroughs enabling the HC-PCF filling process to be monitored on-line (see Fig. 5a). Light from a laser source tuned to a CO_2 absorption line is injected into the HC-PCF through the connectorized end and the transmitted light is monitored at the HC-PCF output using a free-space photodetector. Air in the chamber is then evacuated with a vacuum pump to purge the fiber. After the purging process, the vacuum chamber is loaded with CO_2 at the desired filling pressure (typ. 20 mbar in our case). The CO_2 molecules slowly diffuse into the HC-PCF core through its open end. The fiber filling process can be monitored on-line by scanning the laser source through an absorption line, as illustrated in Fig. 5b.

The required filling time can be fairly well estimated using an analytical model based on the theory of diffusion that takes into account the fiber geometry and length, as well as the gas parameters [29]. The parameters listed in Table 2 for the CO_2 molecule have been considered in the model computation.

For our selected type of HC-PCF with a 3-m length and a CO_2 pressure of 20 mbar, the filling time is estimated to be 78 min (Fig. 6a), which is in good

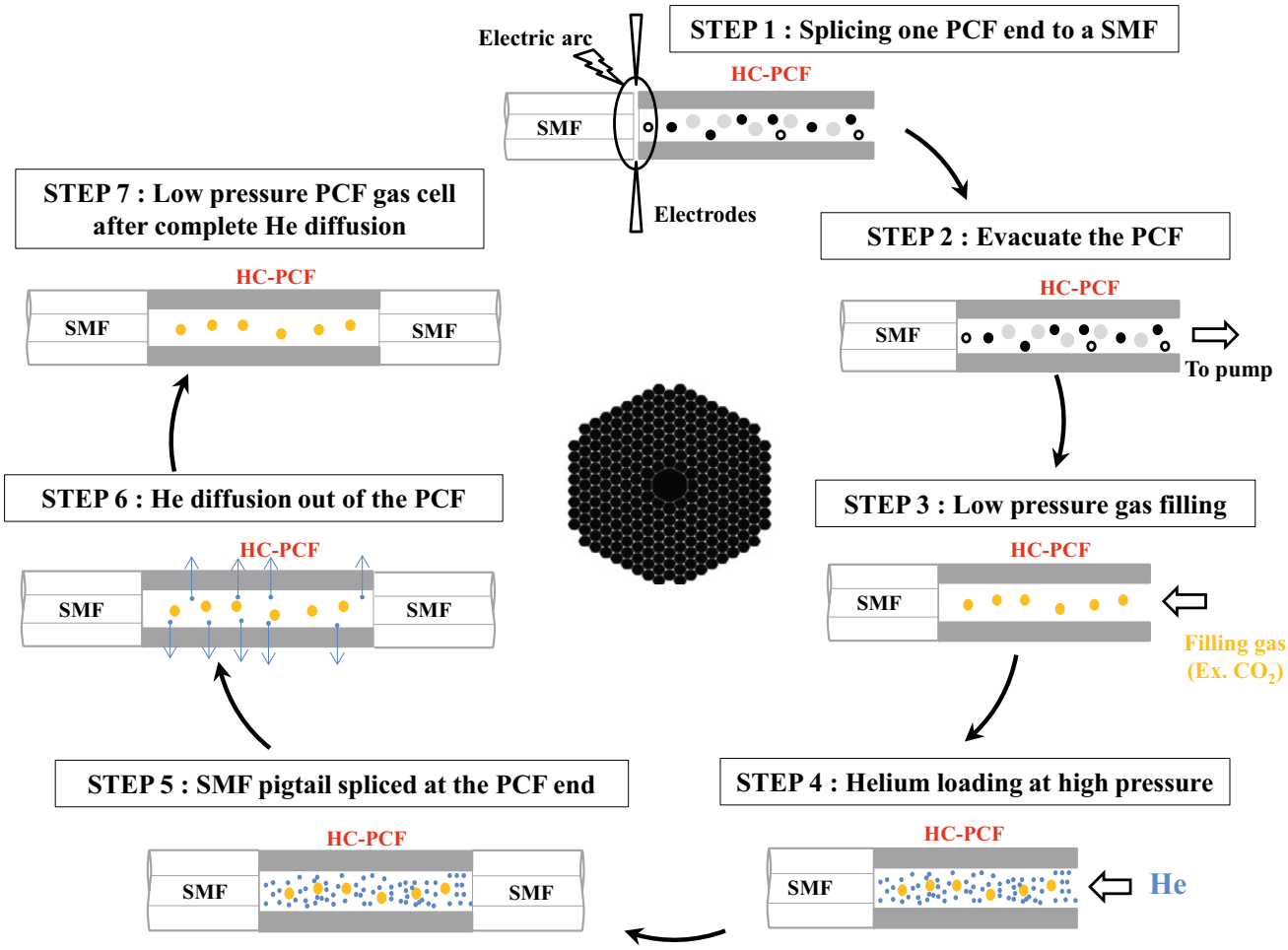

Fig. 4 Applied procedure for the fabrication of a fibered low-pressure gas cell based on an HC-PCF. Polarization maintaining or multimode fibers can also be used instead of SM fibers (SMF) for sealing the cell and coupling light into and out of the HC-PCF. The transverse profile of the used HC-PCF is shown in the center of the figure. The central hole (core) has a diameter of 15 μm

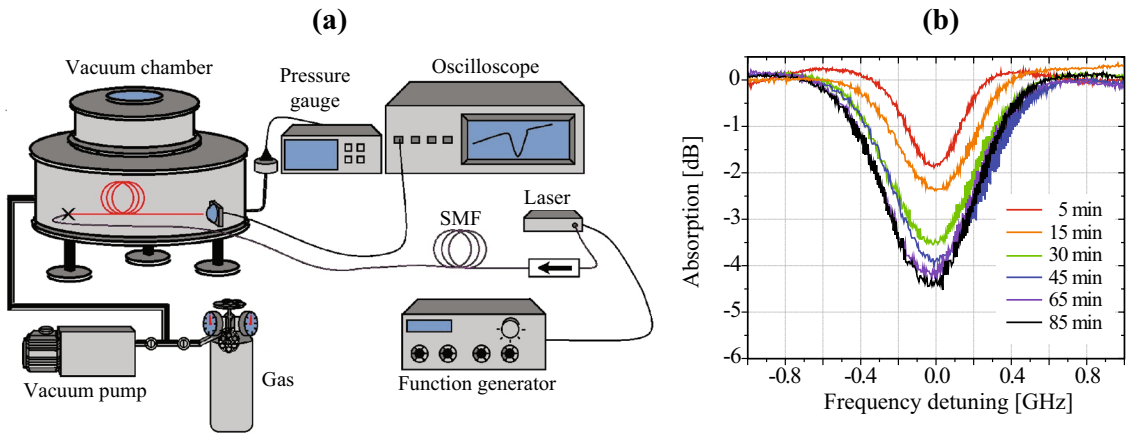

Fig. 5 **a** Scheme of the facilities used for the fabrication of hermetically sealed all-fiber gas reference cells with on-line monitoring. **b** Absorption profiles of the CO_2 R(32) transition at 2050.43 nm measured at different times during the filling process of a 3-m long HC-PCF. A different laser source was used in this characterization, which operated at the R(32) line used here

Table 2 Properties of the carbon dioxide molecule used in the model of the HC-PCF cell filling time [29]

Properties	Symbol	Value
Molecule size	δ	232×10^{-12} m
Molar mass	M	44.01 g mol^{-1}
Molecular mass	$m = M/N_A$	7.31×10^{-26} kg
Mean molecular velocity (273 K)	$\bar{v} = \sqrt{8k_BT/\pi m}$	375.36 m s^{-1}

k_B is the Boltzmann constant, N_A the Avogadro number, T the temperature in the filling system

agreement with the filling time of slightly more than 80 min observed experimentally (Fig. 6b) by monitoring the transmission of the CO_2 R(32) absorption profile for a pressure of ~20 mbar.

Once the HC-PCF is filled with CO_2 at the targeted low pressure, the chamber is loaded with a high pressure of pure helium (typ. 1.7 bar), which rapidly diffuses into the HC-PCF core. Hence, the fiber contains a mixture of CO_2 diluted in a high helium pressure. At this stage, the gas chamber can be opened since air contamination into the HC-PCF core is prevented by the helium overpressure, which will take several minutes to diffuse out of the fiber when exposed to atmospheric conditions. This gives sufficient time to seal the bare end of the HC-PCF by splicing it to a silica fiber. Once the CO_2-filled gas cell is hermetically sealed on both ends, helium gradually permeates out through the thin silica fiber within a couple of hours, leaving behind only the low pressure of pure CO_2 in the HC-PCF core.

3.3 HC-PCF CO_2 cells characterization

The first fabricated fiber gas cells made use of standard 2-μm SM fibers (Nufern SM1950) to seal the cell input and output ports (SM–SM configuration). Spectroscopic measurements reported in Fig. 7a show an absorption profile of the CO_2 R(30) transition with a linewidth (FWHM) in the range of 420–750 MHz and a relative absorption at line-center between 63 and 86%. The variability of these values likely results from an imprecise control of the CO_2 pressure in the vacuum chamber during the HC-PCF filling process. The overall optical transmission of these cells (out of any CO_2 absorption line) reached less than 40%, limited by the splicing losses at the cell input and output. Furthermore, an important interferometric noise pattern was present in the transmission spectra of these SM–SM cells. This pattern was highly sensitive to temperature changes and turned out to depend on the polarization of the light coupled into the HC-PCF. The wavelength-dependent background of the HC-PCF cell resulted in part from a spatial filtering effect at the interface between the multimode HC-PCF and the SM output fiber.

To mitigate the impact of the interferometric noise in the cell transmission spectrum, two different sealing fibers were used in the fabrication process: a polarization-maintaining (PM) fiber (Nufern PM1950) at the cell input and a multimode (MM) fiber at the cell output. This PM–MM configuration mitigated the two aforementioned contributions to the cell transmission background, leading to a reduction of its peak-to-peak amplitude by a factor higher than 2 (see Fig. 7). The sensitive area of the photodiode placed directly at the output of the MM fiber pigtail was

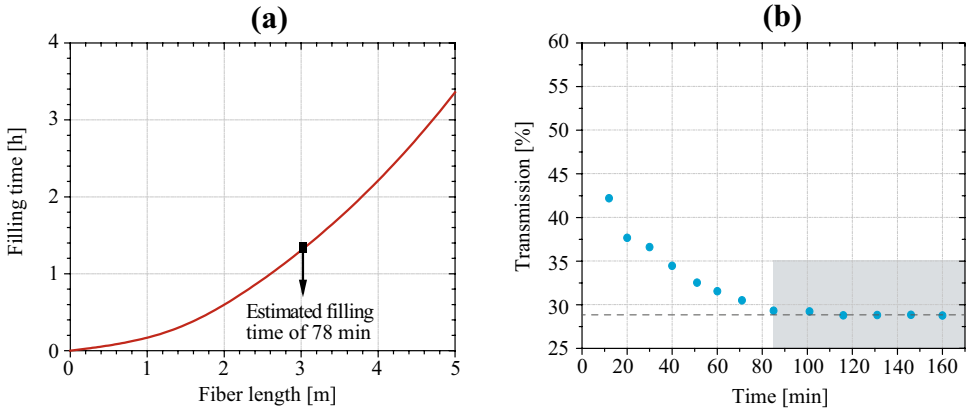

Fig. 6 **a** Predicted filling time as a function of the length of an HC-PCF filled with 20 mbar of CO_2. **b** Temporal evolution of the optical transmission measured at the center of the CO_2 R(32) transition during the filling process of a 3-m long HC-PCF filled with CO_2 at a target pressure of 17.5 mbar. After slightly more than 80 min, the HC-PCF is filled and the absorption reaches its steady-state value (*gray area*). A different laser source was used in this measurement, which operated at the R(32) line used here. However, no significant change in the fiber filling time is expected when measured with the R(30) or R(32) transition

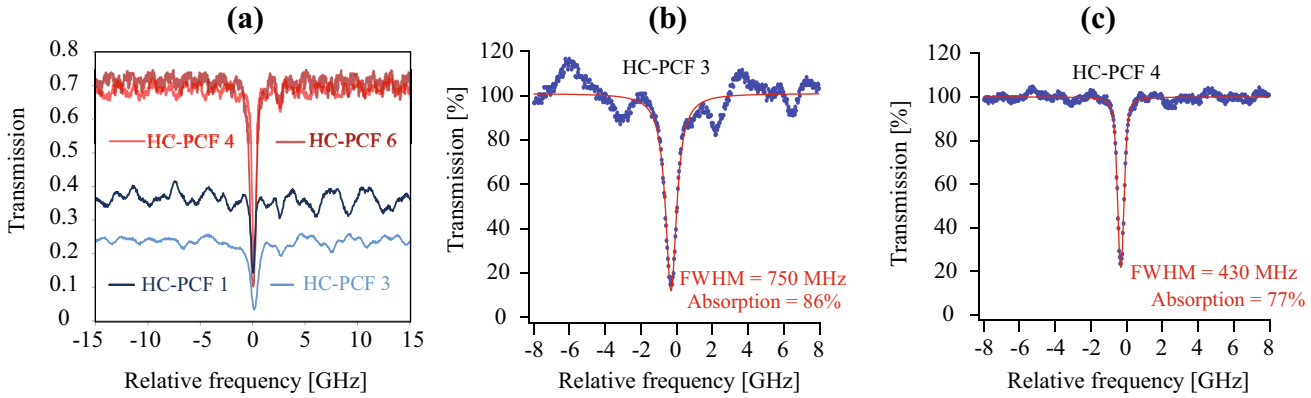

Fig. 7 Transmission spectrum in the vicinity of the CO_2 R(30) transition at 2.051 µm measured for various realizations of HC-PCF cells. Cells 1 and 3 (*blue curves*) are sealed with SM fibers at both input and output ports, while cells 4 and 6 (*red curves*) are sealed with a PM input fiber and an MM output fiber. **a** Overall cell transmission, including splicing losses and fiber attenuation. **b**, **c** Measured relative transmission (*blue points*) and Voigt fit (*red line*) of two HC-PCF gas cells of different geometries: SM–SM (**b**) and PM-MM (**c**) configurations

chosen large enough to collect the entire illumination exiting the output connector of the MM fiber (with 50-µm core diameter). Therefore, the effect of speckle noise arising at the fiber output was totally negligible as the speckle pattern is integrated over the entire beam section. In addition, the use of the MM fiber at the HC-PCF output port significantly improved the overall transmission of the gas cell up to 70%. Finally, it is worth noticing that for each gas cell, comparison of the transmission spectra recorded at an interval of more than 1 year did not reveal any observable change in the cell parameters, indicating that the tightness of the fiber cells is not compromised.

3.4 HC-PCF cell temperature stabilization

The background signal resulting from interferometric noise present in the transmission spectrum of the HC-PCF gas cell and in the error signal may compromise the achievable frequency stability of the laser, as this pattern varies with temperature, resulting in a fluctuating locking point of the laser sideband. To reduce this effect, we have designed a dedicated package to isolate the HC-PCF cell from thermal variations and to actively keep its temperature stable. The effect of temperature on the HC-PCF background signal is illustrated in Fig. 8a for an SM–SM cell configuration that was affected by an important interferometric noise. Figure 8b shows that a reproducible signal is observed from one day to the next at the same cell temperature.

4 Experimental results

4.1 Error signal generation

The parameters of the intensity EOM (carrier frequency, RF input power and DC bias voltage) were adjusted to suppress the optical carrier as described in Sect. 2.2,

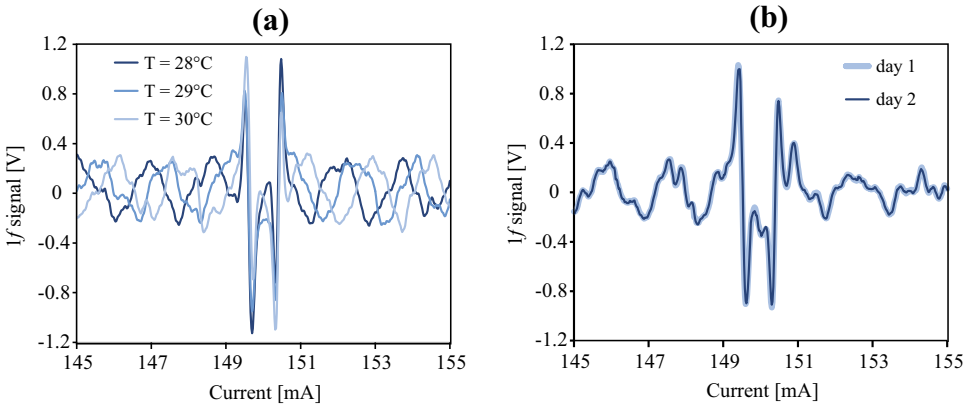

Fig. 8 **a** Variation of the error signal (demodulated signal) of the CO_2 R(30) transition in an HC-PCF cell measured during a current scan of the laser for different temperatures of the fiber housing. **b** Reproducibility between two spectra measured at an interval of 24 h at a constant fiber temperature of 30 °C. The two peaks in the spectra correspond to the interaction of the two modulation sidebands with the CO_2 transition

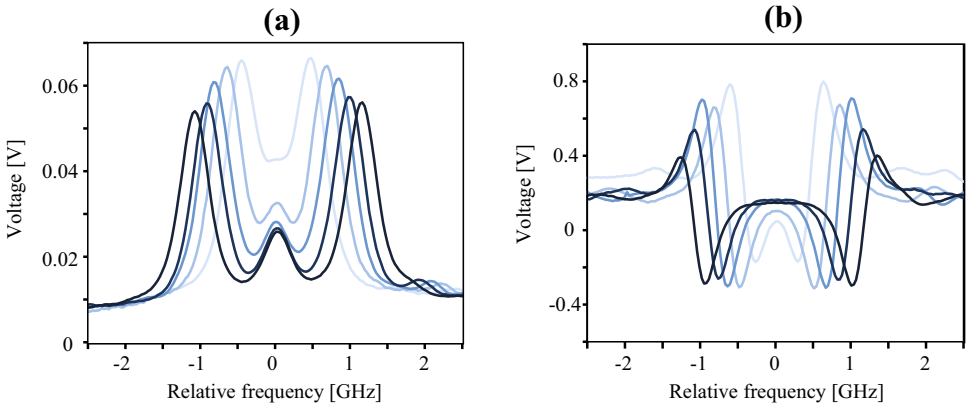

Fig. 9 Transmission spectrum (**a**) and error signal (**b**) of the modulation sideband method obtained for different sideband spacings (~460, 660, 820, 940 and 1100 MHz, from *light to dark blue*) achieved by changing the VCO control voltage and scanning the modulated laser through the CO_2 R(30) line

and to produce a pair of sidebands of maximum amplitude with a frequency separation corresponding to twice the targeted frequency detuning $\Delta\omega_{RF}$ of the laser from the center of the CO_2 transition. Figure 9a illustrates the transmission spectrum of the CO_2 R(30) transition obtained when the EOM output spectrum was tuned through the absorption line by scanning the laser injection current, for different frequency spacing between the sidebands. In this case, the optical carrier was not completely suppressed as a result of the non-optimized DC bias voltage applied to the EOM. The error signal to stabilize one of the sidebands to the center of the CO_2 transition was obtained by frequency-modulating the sidebands (by modulating the input voltage of the VCO at a frequency of ~20 kHz in the present case), and by subsequently demodulating the photodiode signal at the output of the reference gas cell at the same frequency (first harmonic demodulation). Hence, a derivative-like signal of the CO_2 absorption line was obtained for each sideband (see Fig. 9b); no spectral feature occurs at the optical carrier (even if it is incompletely suppressed), since it is not affected by the modulation.

4.2 Balanced detection

To compensate for the RAM resulting from the frequency modulation of the VCO (see discussion in Sect. 2.2), a balanced detection has been implemented using a pair of similar photodiodes. The first photodiode is placed at the output of the reference CO_2 HC-PCF cell and the second one detects a small fraction of the optical power at the output of the EOM (see Fig. 1). The influence of the RAM depends on the modulation frequency of the VCO and creates an offset in the error signal in the case of a single channel detection as illustrated in Fig. 10a. With the use of a balanced detection, this offset is strongly reduced and almost independent of the modulation frequency (Fig. 10b).

4.3 VCO frequency stabilization

The frequency detuning of the laser carrier ω_c from the sideband, stabilized to the CO_2 transition, is directly determined by the frequency ω_{RF} of the EOM driving signal provided by the VCO. To ensure the accuracy of the laser frequency detuning and its long-term stability, the VCO

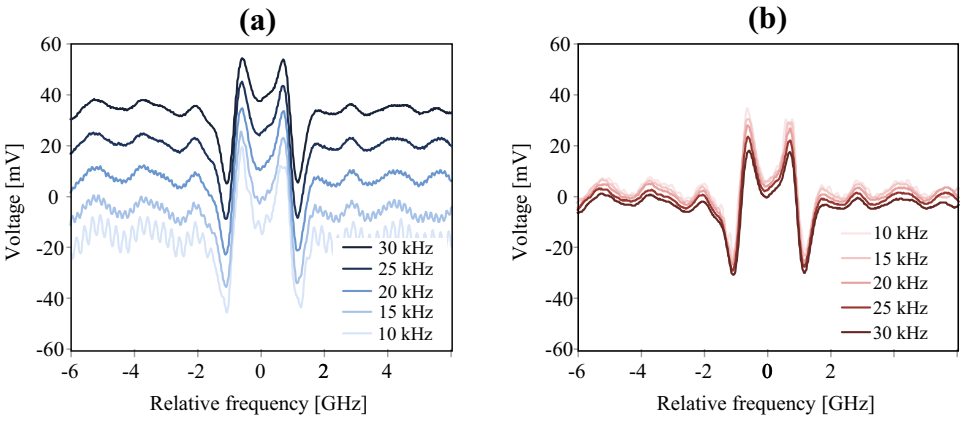

Fig. 10 Variation of the offset in the error signal observed at different modulation frequencies of the VCO in the case of a single channel optical detection (**a**) and of a balanced detection (**b**)

frequency must be locked to a stable RF signal, as it can fluctuate by several hundreds of kilohertz in free-running regime. A stabilization method has been implemented to keep the average VCO frequency ω_{RF} stable and accurate over time even under the large frequency modulation $\Delta\omega_{RF}$ applied for the generation of the error signal for the laser frequency locking (which amounts to a few hundreds of megahertz). It is based on a former similar method developed for an offset-frequency lock between two lasers [16]. For this purpose, part of the VCO output signal is extracted using a power splitter. It is then frequency down-converted by mixing with the reference signal from a stable oscillator and low-pass filtered (using a 50-MHz cut-off frequency filter). Finally, the amplitude of the filtered signal is measured using an envelope detector (Herotek DHM020BB). An error signal for the frequency stabilization of the VCO is obtained by demodulating this signal at the VCO modulation frequency ω_m. The spectral response of the low-pass filter creates a derivative-like error signal that is similar to the error signal of the CO_2 transition used for the laser sideband locking. The effect of the frequency stabilization of the VCO is clearly evident on the long term, for large averaging times, as illustrated in Fig. 11. The achieved instability level of a few kHz or less is sufficient not to impair the targeted frequency stability of the laser (typically tens of kHz).

4.4 Laser stabilization

The performance of the 2-μm laser, stabilized with the developed modulation sideband locking, has been assessed by heterodyning the unmodulated laser carrier with the coherent supercontinuum spectrum generated in a nonlinear fiber from a fully stabilized Er:fiber optical frequency comb (FC1500 from Menlo Systems) referenced to an H-maser, as schematized at the bottom of Fig. 1. The sidebands were generated ~1 GHz away from the carrier and the lower sideband (of smaller frequency) was locked to the CO_2 R(30) transition. The error signal for frequency stabilization was obtained by modulating the VCO driving the EOM with a sine function at 39 kHz, resulting in a peak-to-peak frequency modulation of the sideband of ~225 MHz. The phase of the demodulation was adjusted to maximize the amplitude of the error signal. A PI servo-controller in the home-made laser driver produced the correction signal directly applied to the laser current for stabilization.

We measured the frequency noise power spectral density (FN-PSD) of the laser, both in free-running and

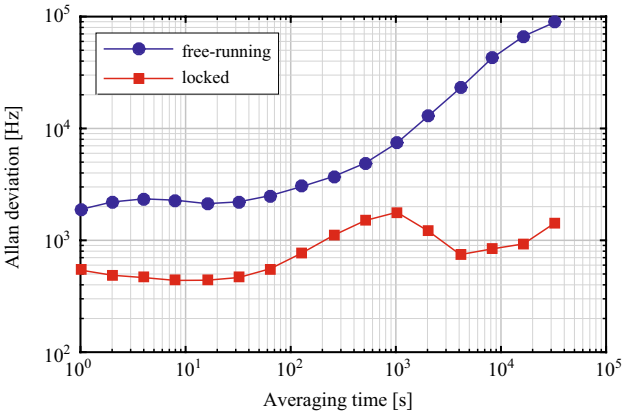

Fig. 11 Demonstration of the frequency stabilization of the VCO used to drive the EOM characterized by its Allan deviation (*blue curve* free-running VCO; *red curve* locked VCO). The VCO frequency (here set around 1 GHz) was measured with a frequency counter, after frequency division by a factor 20 and down-conversion with a mixer to be in the operation range of the counter

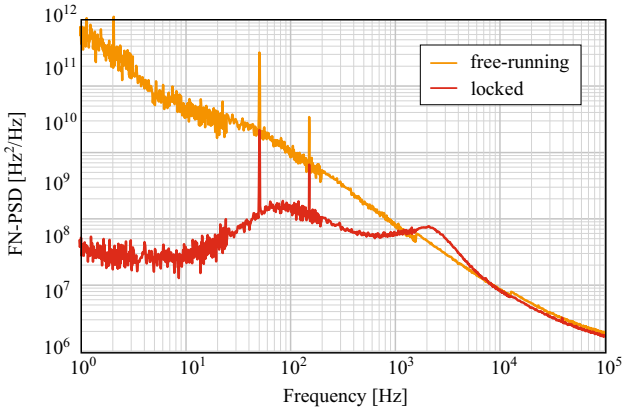

Fig. 12 Frequency noise power spectral density (FN-PSD) of the laser in free-running mode (*orange curve*) and locked (*red curve*). In the locked case, the lower EOM sideband at ω_{RF} ≈1 GHz was stabilized to the CO_2 R(30) transition

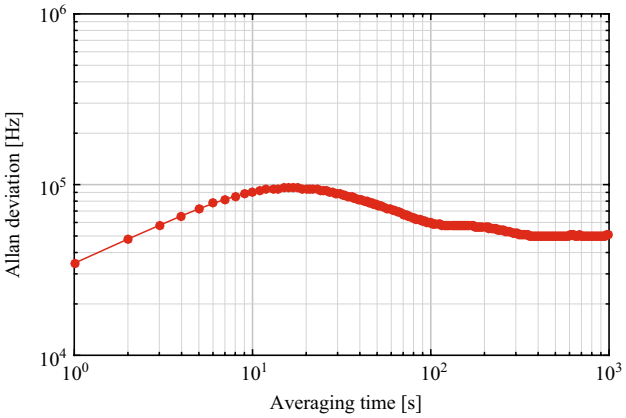

Fig. 13 Frequency stability (Allan deviation) of the laser locked with a detuning of ~1 GHz from the center of the CO_2 R(30) transition using the developed modulation sideband locking scheme

locked conditions, by analyzing the heterodyne beat signal with the frequency comb using a frequency discriminator [30]. Results are displayed in Fig. 12. The frequency noise reduction observed when the stabilization loop is closed corresponds to a feedback bandwidth of ~2.5 kHz.

The frequency stability of the laser was assessed by measuring the frequency of the beat signal with the frequency comb, as well as the repetition rate and carrier–envelope offset frequencies of the comb, using a multichannel Π-type frequency counter without dead-time. Figure 13 shows an Allan deviation below 40 kHz at 1-s integration time and lower than 100 kHz at all timescales up to 1000 s. This complies with the typical requirements of 70–400 kHz above 700-s averaging times and even higher values for shorter averaging times for the reference seed source of a space CO_2 IPDA lidar [10]. A significant degradation of the frequency stability occurs in the range of 1–20 s. It results from interferometric noise in the HC-PCF gas cell that induces a varying background in the error signal for the sideband stabilization, which mainly arises from the multimode nature and the photonics bandgap guiding mechanism of the HC-PCF.

5 Discussion and conclusion

We have developed a frequency-stable continuous-wave seed laser at 2051 nm for a CO_2 IPDA instrument based on a modulation sideband locking scheme. This method enables the only laser present in the setup to be stabilized and frequency detuned from the center of the selected CO_2 R(30) transition. By applying a frequency modulation to the sidebands, an error signal is generated to lock one of them to the center of the CO_2 transition using a modified wavelength modulation spectroscopy technique with first harmonic detection. In this way, a stable laser carrier frequency is achieved with a frequency detuning from the center of the considered transition that is directly controlled by the EOM driving signal. The stable optical carrier, which remains totally free from any superimposed modulation exploited by the tracking and locking module, is pure and constitutes the output of the system to be used for further injection locking of a DIAL pulsed transmitter laser.

To realize a compact, robust, all-fiber setup that is immune to mechanically-induced optical misalignments, an HC-PCF filled at low CO_2 pressure is used as a reference gas cell. Different sealing fibers were tested to ensure the best performance of our fabricated HC-PCF cells. The most appropriate configuration uses a PM fiber at the input port and an MM fiber at the output. It demonstrates improved performance through smaller variations of the cell background spectrum and a higher overall transmission resulting from lower splicing losses. The built all-fiber cells have a length of 3 m and are filled with ~20 mbar of pure CO_2.

Using such a reference gas cell, we have achieved frequency stability (Allan deviation) below 40 kHz at 1-s integration time and lower than 100 kHz at all time scales up to 1000 s. For the purpose of the demonstration, the laser was detuned by around 1 GHz from the center of the CO_2 R(30) transition, but other values ranging from some hundred megahertz to a few gigahertz are also possible. For comparison with other frequency-stabilized lasers in the 2.05-μm wavelength range reported in the literature, we have also calculated a root-mean-square (rms) standard deviation of ~190 kHz for our frequency-stabilized laser over a period of more than 3 h. Koch et al. reported an rms deviation of 870 kHz for a cw solid-state laser frequency-stabilized around 1.2 GHz away from the center of a CO_2 absorption line at 2053 nm [13], whereas Refaat et al. achieved an rms deviation of 650 kHz for a semiconductor laser stabilized to the center of the CO_2 R(30) transition at 2051 nm, as estimated from a statistical analysis and a fitting procedure [14]. One should notice in these comparisons that different measurement instrumentation and data processing were used in each case to retrieve the frequency instability.

The main limitation in the performance of the developed system reported here results from interferometric noise in the HC-PCF gas cell, which is mainly due to the multimode nature and to the photonics bandgap guiding mechanism of the only commercially available HC-PCF at 2 μm that we have used. In a next step, we will investigate the possibility of working with other types of HC-PCFs, such as those based on a Kagomé lattice structure with a hypocycloid core that has demonstrated single mode propagation in the 1.55-μm range [31]. This type of fibers can potentially significantly reduce the interferometric noise in the cell transmission, thereby further improving the laser frequency stability of our proposed modulation sideband locking scheme.

Acknowledgements This work is funded by the European Space Agency (ESTEC contract no. 4000108041/13/NL/PA).

References

1. NASA: Shuttle Atmospheric Lidar Research Program: Final Report of Atmospheric Lidar Working Group. NASA SP No. 433 (Scientific and Technical Information Branch National Aeronautics and Space Administration, 1979)
2. Weitkamp, C. (ed.): Lidar, Range-Resolved Optical Remote Sensing of the Atmosphere, Springer Series in Optical Sciences, vol. 102. Springer, Berlin (2005)
3. Schotland R.M.: Some observation of the vertical profile of water vapor by a laser optical radar. In: Proceedings of 4th Symposium on Remote Sensing of the Environment, pp. 273–283 (1966)

4. Kawa, S.R., Mao, J., Abshire, J.B., Collatz, G.J., Sun, X., Weaver, C.J.: Simulation studies for a space-based CO_2 lidar mission. Tellus B **62**, 759–769 (2010)
5. A-SCOPE (Advanced Space Carbon and Climate Observation of Planet Earth), Report for Assessment ESA SP-1313/1 (2008)
6. Ehret, G., Kiemle, C., Wirth, M., Amediek, A., Fix, A., Houweling, S.: Space-borne remote sensing of CO_2, CH_4, and N_2O by integrated path differential absorption lidar: a sensitivity analysis. Appl. Phys. B **90**, 593–608 (2008)
7. Menzies, R.T., Tratt, D.M.: Differential laser absorption spectrometry for global profiling of tropospheric carbon dioxide: selection of optimum sounding frequencies for high-precision measurements. Appl. Opt. **42**, 6569–6577 (2003)
8. Refaat, T.F., Singh, U.N., Yu, J., Petros, M., Ismail, S., Kavaya, M.J., Davis, K.J.: Evaluation of an airborne triple-pulsed 2 μm IPDA lidar for simultaneous and independent atmospheric water vapor and carbon dioxide measurements. Appl. Opt. **54**, 1387–1398 (2015)
9. Allan, D.W.: Statistics of atomic frequency standards. Proc. IEEE **54**, 221–230 (1966)
10. Fix, A., Matthey, R., Amediek, A., Ehret, G., Gruet, F., Kiemle, C., Klein, V., Mileti, G., Pereira do Carmo, J., Quatrevalet, M.: Investigations on frequency and energy references for a space-borne integrated path differential absorption LIDAR. In: Proceedings ICSO-2014 (ESA Communication, 2014)
11. Matthey, R., Gruet, F., Schilt, S., Mileti, G.: Compact rubidium-stabilized multi-frequency reference source in the 1.55-μm region. Opt. Lett. **40**, 2576–2579 (2015)
12. Matthey, R., Moreno, W., Gruet, F., Brochard, P., Schilt, S., Mileti, G.: Rb-stabilized laser at 1572 nm for CO_2 monitoring. J. Phys. Conf. Ser. **723**, 012034 (2016)
13. Koch, G.J., Beyon, J.Y., Gibert, F., Barnes, B.W., Ismail, S., Petros, M., Petzar, P.J., Yu, J., Modlin, E.A., Davis, K.J., Singh, U.N.: Side-line tunable laser transmitter for differential absorption lidar measurements of CO_2: design and application to atmospheric measurements. Appl. Opt. **47**, 944–956 (2008)
14. Refaat, T.F., Petros, M., Antill, C.W., Singh, U.N., Yu, J.: Wavelength locking to CO_2 absorption line-center for 2-μm pulsed IPDA lidar application. In: Proceedings of SPIE 9879 (Lidar Remote Sensing for Environmental Monitoring XV), pp. 987904–98711 (2016)
15. Bertinetto, F., Bonanni, P., Gambini, P., Puleo, M., Vezzoni, E.: Performance and limitations of laser diodes stabilized to the sides of molecular absorption lines of ammonia. Rev. Sci. Instrum. (1998)
16. Schilt, S., Matthey, R., Kauffmann-Werner, D., Affolderbach, C., Mileti, G., Thévenaz, L.: Laser offset-frequency locking up to 20 GHz using a low-frequency electrical filter technique. Appl. Opt. **47**, 4336–4344 (2008)
17. Bernard, V., Daussy, C., Nogues, G., Constantin, L., Durand, P.E., Amy-Klein, A., Van Lerberghe, A., Chardonnet, C.: CO_2 laser stabilization to 0.1-Hz level using external electrooptic modulation. IEEE J. Quantum Electron. **33**, 1282–1287 (1997)
18. Nevsky, A., Alighanbari, S., Chen, Q.-F., Ernsting, I., Vasilyev, S., Schiller, S., Barwood, G., Gill, P., Poli, N., Tino, G.M.: Robust frequency stabilization of multiple spectroscopy lasers with large and tunable offset frequencies. Opt. Lett. **38**, 4903–4906 (2013)
19. Thorpe, J.I., Numata, K., Livas, J.: Laser frequency stabilization and control through offset sideband locking to optical cavities. Opt. Express **16**, 15980–15990 (2008)
20. Cregan, R.F., Mangan, B.J., Knight, J.C., Birks, T.A., Russell, P.S.J., Roberts, P.J., Allan, D.C.: Single-mode photonic band gap guidance of light in air. Science **285**, 1537–1539 (1999)
21. Benabid, F., Couny, F., Knight, J.C., Birks, T.A., Russell, P.S.J.: Compact, stable and efficient all-fibre gas cells using hollow-core photonic crystal fibres. Nature **434**, 488–491 (2005)
22. Dicaire, I.: Optical gas-phase frequency references based on photonic crystal technology: impact of slow light on molecular absorption. PhD Dissertation (EPFL, 2012)
23. Supplee, J.M., Whittaker, E.A., Lenth, W.: Theoretical description of frequency modulation and wavelength modulation spectroscopy. Appl. Opt. **33**, 6294–6302 (1994)
24. Burkart, J., Romanini, D., Kassi, S.: Optical feedback stabilized laser tuned by single-sideband modulation. Opt. Lett. **38**, 2062 (2013)
25. Bomse, D.S., Stanton, A.C., Silver, J.A.: Frequency modulation and wavelength modulation spectroscopies: comparison of experimental methods using a lead-salt diode laser. Appl. Opt. **31**, 718–731 (1992)
26. Rothman, L.S., Gordon, I.E., Barbe, A., Benner, D.C., Bernath, P.F., Birk, M., Boudon, V., Brown, L.R., Campargue, A., Champion, J.-P., Chance, K., Coudert, L.H., Dana, V., Devi, V.M., Fally, S., Flaud, J.-M., Gamache, R.R., Goldman, A., Jacquemart, D., Kleiner, I., Lacome, N., Lafferty, W.J., Mandin, J.-Y., Massie, S.T., Mikhailenko, S.N., Miller, C.E., Moazzen-Ahmadi, N., Naumenko, O.V., Nikitin, A.V., Orphal, J., Perevalov, V.I., Perrin, A., Predoi-Cross, A., Rinsland, C.P., Rotger, M., Šimečková, M., Smith, M.A.H., Sung, K., Tashkun, S.A., Tennyson, J., Toth, R.A., Vandaele, A.C., Vander Auwera, J.: The HITRAN 2008 molecular spectroscopic database. J. Quant. Spectrosc. Radiat. Transf. **110**, 533–572 (2009)
27. Li, J., Durry, G., Cousin, J., Joly, L., Parvitte, B., Zeninari, V.: Self-induced pressure shift and temperature dependence measurements of CO_2 at 2.05 μm with a tunable diode laser spectrometer. Spectrochim. Acta. A. Mol. Biomol. Spectrosc. **85**, 74–78 (2012)
28. Light, P.S., Couny, F., Benabid, F.: Low optical insertion-loss and vacuum-pressure all-fiber acetylene cell based on hollow-core photonic crystal fiber. Opt. Lett. **31**, 2538–2540 (2006)
29. Dicaire, I., Beugnot, J.-C., Thévenaz, L.: Analytical modeling of the gas-filling dynamics in photonic crystal fibers. Appl. Opt. **49**, 4604–4609 (2010)
30. Schilt, S., Bucalovic, N., Tombez, L., Dolgovskiy, V., Schori, C., Di Domenico, G., Zaffalon, M., Thomann, P.: Frequency discriminators for the characterization of narrow-spectrum heterodyne beat signals: application to the measurement of a sub-hertz carrier-envelope-offset beat in an optical frequency comb. Rev. Sci. Instrum. **82**, 123116 (2011)
31. Wang, Y., Alharbi, M., Bradley, T.D., Fourcade-Dutin, C., Debord, B., Beaudou, B., Gerôme, F., Benabid, F.: Hollow-core photonic crystal fibre for high power laser beam delivery. High Power Laser Sci. Eng. **1**, 17–28 (2013)